Available online at www.sciencedirect.com

SCIENCE @ DIRECT®

European Journal of Mechanics B/Fluids 24 (2005) 338–352

Investigation of laminar flow in a helical pipe filled with a fluid saturated porous medium

L. Cheng, A.V. Kuznetsov *

Department of Mechanical and Aerospace Engineering, North Carolina State University, Campus Box 7910, Raleigh, NC 27695-7910, USA

Received 24 March 2004; received in revised form 18 August 2004; accepted 25 August 2004

Abstract

Laminar flow in a helical pipe filled with a fluid saturated porous medium is investigated numerically. The analysis is based on a full momentum equation for the flow in porous media that accounts for the Brinkman and Forchheimer extensions of the Darcy law as well as for the flow inertia. Accounting for the flow inertia is shown to be important for predicting secondary flow in a helical pipe. The effects of the Darcy number, the Forchheimer coefficient as well as the curvature and torsion of the helical pipe on the axial flow velocity and secondary flow are investigated numerically.

Keywords: Helical pipe; Porous medium; Laminar flow; Orthogonal helical coordinates

1. Introduction

Flow in helical pipes has been a subject of intensive investigation. The major advantage of helical pipe flow is the occurrence of a secondary flow in planes normal to the main flow. Secondary flow increases heat and mass transfer efficiency compared to that in straight pipes. Dean [1] initially studied the flow in loosely coiled pipes and found the secondary flow with two symmetric vortices. Besides the Reynolds number, *Re*, another parameter, the Dean number, *Dn*, was later introduced to characterize the magnitude and the shape of the secondary flow. Germano [2,3] suggested an orthogonal helical coordinate system and used it to solve a laminar flow problem with a small ratio of torsion to curvature. He concluded that torsion has a second-order effect on the helical pipe flow. The Germano number, *Gn*, was introduced by Liu and Masliyah [4]. The Dean number given by $Dn = \varepsilon^{1/2} Re$ is a measure of the ratio of the square root of the product of inertial and centrifugal forces to the viscous forces. The Germano number given by $Gn = (\varepsilon\lambda) Re$ is a measure of the ratio of the centrifugal forces to the viscous forces (Liu and Masliyah [5]). Liu and Masliyah [4,5] performed a comprehensive analysis of fully-developed laminar Newtonian flows in helical pipes of constant circular cross-sections with a finite pitch and found that when the torsion is dominant, the flow in helical pipes approaches that in a straight pipe. When the torsion is small, the developing flow is oscillatory and the flow develops more quickly than in a straight pipe. Numerical studies have been conducted later to examine the effects of torsion and curvature on the fluid flow in helical pipes [6–11].

---

* Corresponding author. Tel.: +1-919-515-2365; fax: +1-919-515-7968.
E-mail address: avkuznet@eos.ncsu.edu (A.V. Kuznetsov).

0997-7546/$ – see front matter
doi:10.1016/j.euromechflu.2004.08.002

Nomenclature

a	pipe radius, m
C_F	Forchheimer coefficient
Da	Darcy number, K/a^2
Dn	Dean number, $\varepsilon^{1/2}Re$
g	gravity, m/s^2
Gn	Germano number, $(\varepsilon\lambda)Re$
h_s	dimensionless scale factor
$\tilde{h}_r, \tilde{h}_s, \tilde{h}_\theta$	dimensional scale factors
K	permeability, m^2
Re	Reynolds number, $\rho_f U a/\mu$
r	dimensionless radial coordinate, $\tilde{r}/a$
$\tilde{r}$	radial coordinate, m
$\hat{\mathbf{r}}$	residual vector
s	dimensionless axial coordinate, $\tilde{s}/a$
$\tilde{s}$	axial coordinate, m
p	pitch, m
P	dimensionless pressure, $\widetilde{P}/\rho U^2$
$\widetilde{P}$	pressure, Pa
U	bulk velocity, defined in Eq. (2.9), m/s
$\tilde{\mathbf{v}}$	velocity vector, m/s
u_s, u_r, u_θ	dimensionless velocity components, $\tilde{u}_s/U$, $\tilde{u}_r/U$, $\tilde{u}_\theta/U$
$\tilde{u}_s, \tilde{u}_r, \tilde{u}_\theta$	velocity components, m s^{-1}

Greek symbols

ε	dimensionless curvature, κa
θ	angle, defined in Fig. 1(b)
κ	curvature, m^{-1}
λ	the ratio of torsion to curvature, τ/κ
μ	effective dynamic viscosity of the porous medium (assumed to the same as the fluid viscosity), kg m^{-1} s^{-1}
ν	effective kinematic viscosity in a porous medium, m^2 s^{-1}
ξ	angle, defined in Eq. (2.10)
ρ_f	fluid density, kg m^{-3}
τ	torsion, m^{-1}
φ	porosity
ϕ	angle, defined in Eq. (2.3)

Subscripts

s	axial direction
r	radial direction
θ	circumferential direction

Sandeep [12] extended the analysis of helical pipe flow to non-Newtonian fluids; the numerical research was performed in a Cartesian coordinate system. Cheng and Kuznetsov [13] used the orthogonal helical coordinate system to study the effects of torsion and curvature on non-Newtonian fluid flow in helical pipes and compared the flow dynamics between Newtonian and non-Newtonian fluids.

Nield and Kuznetsov [14] presented a perturbation analysis and obtained an analytical expression for the Nusselt number in a helical pipe filled with a porous medium for the case when flow in a pipe is described by the Darcy law. Except for this paper, to the best of the authors' knowledge, nothing has been published on flows in helical pipes filled with a fluid saturated porous medium. The aim of the present paper is to fill this gap in the literature. Flow in helical pipes filled with a fluid saturated porous medium is relevant to a number of engineering and biological applications, such as the flow in a helical segment of clotted human coronary artery. This paper investigates laminar flow in a helical pipe filled with a porous medium. Since the secondary flow in a helical pipe becomes significant at relatively large flow velocity, it is insufficient to describe the drag that the porous medium imposes on a fluid by using just one linear (Darcy) term; at larger filtration velocities the surface drag due to friction becomes comparable with the form drag due to solid obstacles (Nield and Bejan [15]). Since the form drag due to solid obstacles is proportional to the square of the filtration velocity, to account for this effect an additional quadratic drag term is introduced into the momentum equation, which is called the Forchheimer term. In this paper, the most general form of a momentum equation for porous media, the Brinkman–Forchheimer-extended Darcy equation with inertia terms, is utilized; this equation is solved numerically in an orthogonal helical coordinate system suggested by Germano [2,3]. The geometry of a helical pipe is characterized by the curvature and torsion. In this study, the effects of the Darcy number, the Forchheimer coefficient, the curvature and torsion of the helical pipe on the axial flow velocity and secondary flow are investigated numerically. The investigation shows that increasing the Darcy number increases the distortion of the axial velocity profile and enhances the secondary flow. Increasing the Forchheimer coefficient decreases the axial velocity and the secondary flow. The dimensionless curvature of helical pipes affects both the axial velocity distribution and the secondary flow, but the ratio of torsion to curvature produces a noticeable effect only on the secondary flow.

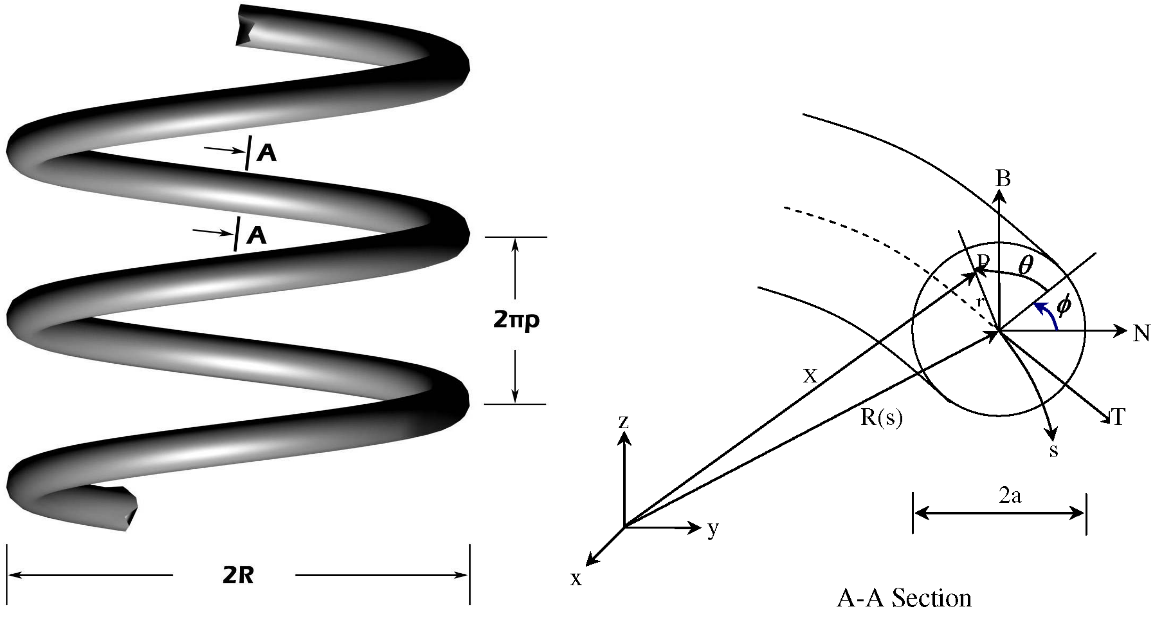

(a) (b)

Fig. 1. (a) Schematic diagram of a helical pipe. (b) The orthogonal helical coordinate system.

2. Governing equations

Fig. 1(a) shows the schematic diagram of a helical pipe which is characterized by two parameters, the curvature, κ, and the torsion, τ, which are defined as, respectively

$$\kappa = \frac{R}{R^2 + p^2}, \qquad \tau = \frac{p}{R^2 + p^2}. \tag{2.1}$$

Fig. 1(b) displays the orthogonal helical coordinate system introduced by Germano [2,3] with the helical coordinate s for the axial direction, r for the radial direction, and θ for the circumferential direction. The metric for this coordinate system is given by

$$\mathrm{d}\mathbf{x} \cdot \mathrm{d}\mathbf{x} = \left[1 + \kappa \tilde{r} \sin(\theta + \phi)\right]^2 (d\tilde{s})^2 + (d\tilde{r})^2 + \tilde{r}^2 (\mathrm{d}\theta)^2, \tag{2.2}$$

where

$$\phi(\tilde{s}) = -\int_{\tilde{s}_0}^{\tilde{s}} \tau(\tilde{s}')\,\mathrm{d}\tilde{s}'. \tag{2.3}$$

The continuity and momentum equations in the vector form are

$$\nabla \cdot \tilde{\mathbf{v}} = 0 \tag{2.4}$$

and

$$\frac{\rho_f}{\varphi^2}(\tilde{\mathbf{v}} \cdot \nabla)\tilde{\mathbf{v}} = -\nabla \widetilde{P} + \frac{\mu}{\varphi}\nabla^2 \tilde{\mathbf{v}} - \frac{\mu}{K}\tilde{\mathbf{v}} - \frac{C_{\mathrm{F}}\rho_f}{K^{1/2}}|\tilde{\mathbf{v}}|\tilde{\mathbf{v}}, \tag{2.5}$$

where K is the permeability of the porous medium, C_{F} is the Forchheimer coefficient, and φ is the porosity.

Eq. (2.5) is a full momentum equation for the steady flow in porous media that accounts for the Brinkman and Forchheimer extensions of the Darcy law as well as for the flow inertia [15].

In the orthogonal helical coordinate system, the scale factors are given by

$$\tilde{h}_s = 1 + \kappa \tilde{r} \sin(\theta + \phi), \qquad \tilde{h}_r = 1, \qquad \tilde{h}_\theta = \tilde{r}. \tag{2.6}$$

The dimensionless governing equations for the flow in a porous medium written in the orthogonal helical coordinate system are the continuity equation

$$\frac{\partial(ru_s)}{\partial s}+\frac{\partial(rh_su_r)}{\partial r}+\frac{\partial(h_su_\theta)}{\partial\theta}=0 \tag{2.7}$$

and the momentum equations

$$\begin{aligned}&\frac{1}{\varphi^2}\frac{1}{h_sr}\left(\frac{\partial(ru_su_s)}{\partial s}+\frac{\partial(rh_su_ru_s)}{\partial r}+\frac{\partial(h_su_\theta u_s)}{\partial\theta}\right)+\frac{1}{\varphi^2}\frac{\varepsilon}{h_s}u_s\big(u_r\sin(\theta+\phi)+u_\theta\cos(\theta+\phi)\big)\\&\quad=-\frac{1}{h_s}\frac{\partial P}{\partial s}+\frac{1}{\varphi}\frac{1}{Re}\left\{\frac{1}{h_s}\frac{\partial}{\partial s}\left[\frac{1}{h_sr}\left[\frac{\partial(ru_s)}{\partial s}+\frac{\partial(rh_su_r)}{\partial r}+\frac{\partial(h_su_\theta)}{\partial\theta}\right]\right]\right.\\&\qquad\left.-\frac{1}{r}\left(\frac{\partial}{\partial r}\left(\frac{r}{h_s}\left(\frac{\partial u_r}{\partial s}-\frac{\partial}{\partial r}(h_su_s)\right)\right)-\frac{\partial}{\partial\theta}\left(\frac{1}{h_sr}\left(\frac{\partial}{\partial\theta}(h_su_s)-\frac{\partial}{\partial\theta}(ru_\theta)\right)\right)\right)\right\}\\&\qquad-\frac{1}{Re}\frac{1}{Da}u_s-\frac{C_{\mathrm{F}}}{Da^{1/2}}u_s(u_s^2+u_r^2+u_\theta^2)^{1/2},\end{aligned}\tag{2.8a}$$

$$\begin{aligned}&\frac{1}{\varphi^2}\frac{1}{h_sr}\left(\frac{\partial(ru_su_r)}{\partial s}+\frac{\partial(rh_su_ru_r)}{\partial r}+\frac{\partial(h_su_\theta u_r)}{\partial\theta}\right)-\frac{1}{\varphi^2}\frac{u_\theta^2}{r}-\frac{1}{\varphi^2}\frac{\varepsilon}{h_s}u_s^2\sin(\theta+\phi)\\&\quad=-\frac{\partial P}{\partial r}+\frac{1}{\varphi}\frac{1}{Re}\left\{\frac{\partial}{\partial r}\left[\frac{1}{h_sr}\left[\frac{\partial(ru_s)}{\partial s}+\frac{\partial(rh_su_r)}{\partial r}+\frac{\partial(h_su_\theta)}{\partial\theta}\right]\right]\right.\\&\qquad\left.-\frac{1}{h_sr}\left(\frac{\partial}{\partial\theta}\left(\frac{h_s}{r}\left(\frac{\partial}{\partial r}(ru_\theta)-\frac{\partial u_r}{\partial\theta}\right)\right)-\frac{\partial}{\partial s}\left(\frac{r}{h_s}\left(\frac{\partial u_r}{\partial s}-\frac{\partial}{\partial r}(h_su_s)\right)\right)\right)\right\}\\&\qquad-\frac{1}{Re}\frac{1}{Da}u_r-\frac{C_{\mathrm{F}}}{Da^{1/2}}u_r(u_s^2+u_r^2+u_\theta^2)^{1/2},\end{aligned}\tag{2.8b}$$

$$\begin{aligned}&\frac{1}{\varphi^2}\frac{1}{h_sr}\left(\frac{\partial(ru_su_\theta)}{\partial s}+\frac{\partial(rh_su_ru_\theta)}{\partial r}+\frac{\partial(h_su_\theta u_\theta)}{\partial\theta}\right)-\frac{1}{\varphi^2}\frac{\varepsilon}{h_s}u_s^2\cos(\theta+\phi)+\frac{1}{\varphi^2}\frac{u_ru_\theta}{r}\\&\quad=-\frac{1}{r}\frac{\partial P}{\partial\theta}+\frac{1}{\varphi}\frac{1}{Re_F}\left\{\frac{1}{r}\frac{\partial}{\partial\theta}\left[\frac{1}{h_sr}\left[\frac{\partial(ru_s)}{\partial s}+\frac{\partial(rh_su_r)}{\partial r}+\frac{\partial(h_su_\theta)}{\partial\theta}\right]\right]\right.\\&\qquad\left.-\frac{1}{h_s}\left(\frac{\partial}{\partial s}\left(\frac{1}{h_sr}\left(\frac{\partial}{\partial\theta}(h_su_s)-\frac{\partial}{\partial s}(ru_\theta)\right)\right)-\frac{\partial}{\partial r}\left(\frac{h_s}{r}\left(\frac{\partial}{\partial r}(ru_\theta)-\frac{\partial u_r}{\partial\theta}\right)\right)\right)\right\}\\&\qquad-\frac{1}{Re}\frac{1}{Da}u_\theta-\frac{C_{\mathrm{F}}}{Da^{1/2}}u_\theta(u_s^2+u_r^2+u_\theta^2)^{1/2},\end{aligned}\tag{2.8c}$$

where

$$\begin{aligned}&s=\frac{\tilde s}{a},\quad r=\frac{\tilde r}{a},\quad (u_s,u_r,u_\theta)=\left(\frac{\tilde u_s}{U},\frac{\tilde u_r}{U},\frac{\tilde u_\theta}{U}\right),\quad P=\frac{\widetilde{P}}{\rho_fU^2},\quad \varepsilon=\kappa a,\quad \lambda=\frac{\tau}{\kappa},\\&h_s=1+\varepsilon r\sin(\theta+\phi),\quad Re=\frac{\rho_fUa}{\mu},\quad Da=\frac{K}{a^2},\quad U=\frac{1}{\pi}\int_0^{2\pi}\int_0^1u_sr\,\mathrm{d}r\,\mathrm{d}\theta,\end{aligned}\tag{2.9}$$

where a is the radius of the pipe, and U is the bulk velocity defined in Eq. (2.9).

A fully developed laminar flow is considered so that the dynamic variables except for the pressure are independent of s, therefore, a simplifying transformation is performed from s, r, θ to s, r, ξ:

$$\theta+\phi\Rightarrow\xi,\ \frac{\partial}{\partial s}\Rightarrow\frac{\partial}{\partial s}-\varepsilon\lambda\frac{\partial}{\partial\xi},\ \frac{\partial}{\partial\theta}\Rightarrow\frac{\partial}{\partial\xi}.\tag{2.10}$$

The governing equations are then reduced as:

$$-\varepsilon\lambda\frac{\partial(ru_s)}{\partial\xi}+\frac{\partial(rh_su_r)}{\partial r}+\frac{\partial(h_su_\theta)}{\partial\xi}=0,\tag{2.11}$$

$$\begin{aligned}
&\frac{1}{\varphi^2}\frac{1}{h_s r}\left(-\varepsilon\lambda\frac{\partial(ru_su_s)}{\partial\xi}+\frac{\partial(rh_su_ru_s)}{\partial r}+\frac{\partial(h_su_\theta u_s)}{\partial\xi}\right)+\frac{1}{\varphi^2}\frac{\varepsilon}{h_s}u_s(u_r\sin\xi+u_\theta\cos\xi)\\
&\quad=-\frac{1}{h_s}\left(\frac{\partial P}{\partial s}-\varepsilon\lambda\frac{\partial P}{\partial\xi}\right)+\frac{1}{\varphi}\frac{1}{Re}\left\{-\varepsilon\lambda\frac{1}{h_s}\frac{\partial}{\partial\xi}\left[\frac{1}{h_sr}\left[-\varepsilon\lambda\frac{\partial(ru_s)}{\partial\xi}+\frac{\partial(rh_su_r)}{\partial r}+\frac{\partial(h_su_\theta)}{\partial\xi}\right]\right]\right.\\
&\quad\quad\left.-\frac{1}{r}\left(\frac{\partial}{\partial r}\left(\frac{r}{h_s}\left(-\varepsilon\lambda\frac{\partial u_r}{\partial\xi}-\frac{\partial}{\partial r}(h_su_s)\right)\right)-\frac{\partial}{\partial\xi}\left(\frac{1}{h_sr}\left(\frac{\partial}{\partial\xi}(h_su_s)+\varepsilon\lambda\frac{\partial}{\partial\xi}(ru_\theta)\right)\right)\right)\right\}\\
&\quad\quad-\frac{1}{Re}\frac{1}{Da}u_s-\frac{C_\mathrm{F}}{Da^{1/2}}u_s(u_s^2+u_r^2+u_\theta^2)^{1/2},
\end{aligned}\tag{2.12a}$$

$$\begin{aligned}
&\frac{1}{\varphi^2}\frac{1}{h_s r}\left(-\varepsilon\lambda\frac{\partial(ru_su_r)}{\partial\xi}+\frac{\partial(rh_su_ru_r)}{\partial r}+\frac{\partial(h_su_\theta u_r)}{\partial\xi}\right)-\frac{1}{\varphi^2}\frac{u_\theta^2}{r}-\frac{1}{\varphi^2}\frac{\varepsilon}{h_s}u_s^2\sin\xi\\
&\quad=-\frac{\partial P}{\partial r}+\frac{1}{\varphi}\frac{1}{Re}\left\{\frac{\partial}{\partial r}\left[\frac{1}{h_sr}\left[-\varepsilon\lambda\frac{\partial(ru_s)}{\partial\xi}+\frac{\partial(rh_su_r)}{\partial r}+\frac{\partial(h_su_\theta)}{\partial\xi}\right]\right]\right.\\
&\quad\quad\left.-\frac{1}{h_sr}\left(\frac{\partial}{\partial\xi}\left(\frac{h_s}{r}\left(\frac{\partial}{\partial r}(ru_\theta)-\frac{\partial u_r}{\partial\xi}\right)\right)+\varepsilon\lambda\frac{\partial}{\partial\xi}\left(\frac{r}{h_s}\left(-\varepsilon\lambda\frac{\partial u_r}{\partial\xi}-\frac{\partial}{\partial r}(h_su_s)\right)\right)\right)\right\}\\
&\quad\quad-\frac{1}{Re}\frac{1}{Da}u_r-\frac{C_\mathrm{F}}{Da^{1/2}}u_r(u_s^2+u_r^2+u_\theta^2)^{1/2},
\end{aligned}\tag{2.12b}$$

$$\begin{aligned}
&\frac{1}{\varphi^2}\frac{1}{h_s r}\left(-\varepsilon\lambda\frac{\partial(ru_su_\theta)}{\partial\xi}+\frac{\partial(rh_su_ru_\theta)}{\partial r}+\frac{\partial(h_su_\theta u_\theta)}{\partial\xi}\right)-\frac{1}{\varphi^2}\frac{\varepsilon}{h_s}u_s^2\cos\xi+\frac{1}{\varphi^2}\frac{u_ru_\theta}{r}\\
&\quad=-\frac{1}{r}\frac{\partial P}{\partial\xi}+\frac{1}{\varphi}\frac{1}{Re}\left\{\frac{1}{r}\frac{\partial}{\partial\xi}\left[\frac{1}{h_sr}\left[-\varepsilon\lambda\frac{\partial(ru_s)}{\partial\xi}+\frac{\partial(rh_su_r)}{\partial r}+\frac{\partial(h_su_\theta)}{\partial\xi}\right]\right]\right.\\
&\quad\quad\left.-\frac{1}{h_s}\left(-\varepsilon\lambda\frac{\partial}{\partial\xi}\left(\frac{1}{h_sr}\left(\frac{\partial}{\partial\xi}(h_su_s)+\varepsilon\lambda\frac{\partial}{\partial\xi}(ru_\theta)\right)\right)-\frac{\partial}{\partial r}\left(\frac{h_s}{r}\left(\frac{\partial}{\partial r}(ru_\theta)-\frac{\partial}{\partial\xi}(u_r)\right)\right)\right)\right\}\\
&\quad\quad-\frac{1}{Re}\frac{1}{Da}u_\theta-\frac{C_\mathrm{F}}{Da^{1/2}}u_\theta(u_s^2+u_r^2+u_\theta^2)^{1/2}.
\end{aligned}\tag{2.12c}$$

3. Computational procedure

The governing equations are discretized based on a control volume method on an evenly spaced 41 by 41 mesh. The convection–diffusion terms are discretized with the power-law scheme (Patankar [16]) and the other terms are approximated

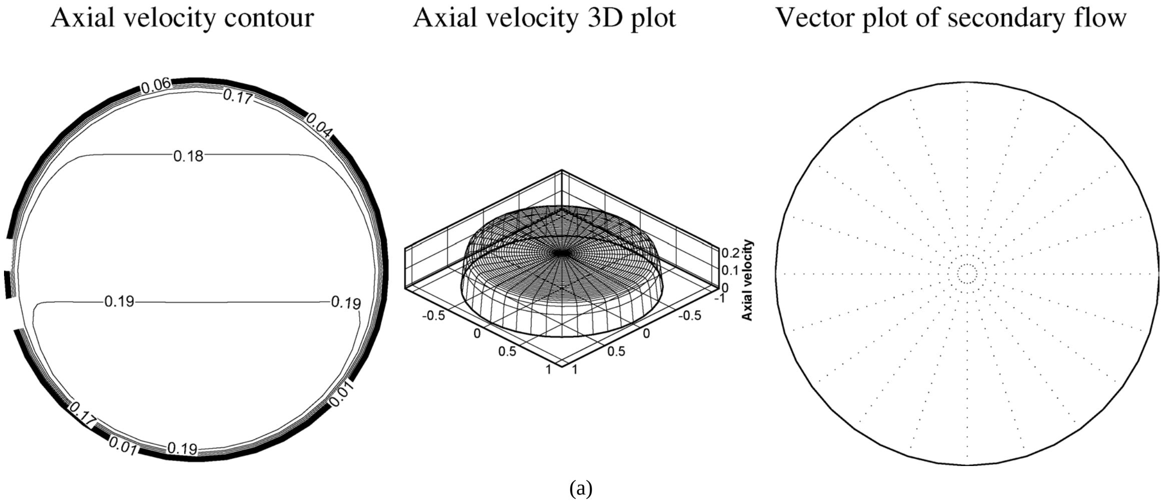

(a)

Fig. 2. Contour lines and 3D plot of the axial velocity and vector plots of the secondary flow at $\mathrm{d}P/\mathrm{d}s=-10$, $C_\mathrm{F}=0.55$, $\varphi=0.95$, $\varepsilon=0.1$, $\lambda=0.1$ for different Darcy numbers: (a) $Da=5\times10^{-4}$, (b) $Da=1\times10^{-3}$, (c) $Da=5\times10^{-3}$, (d) $Da=1\times10^{-2}$, (e) $Da=5\times10^{-2}$.

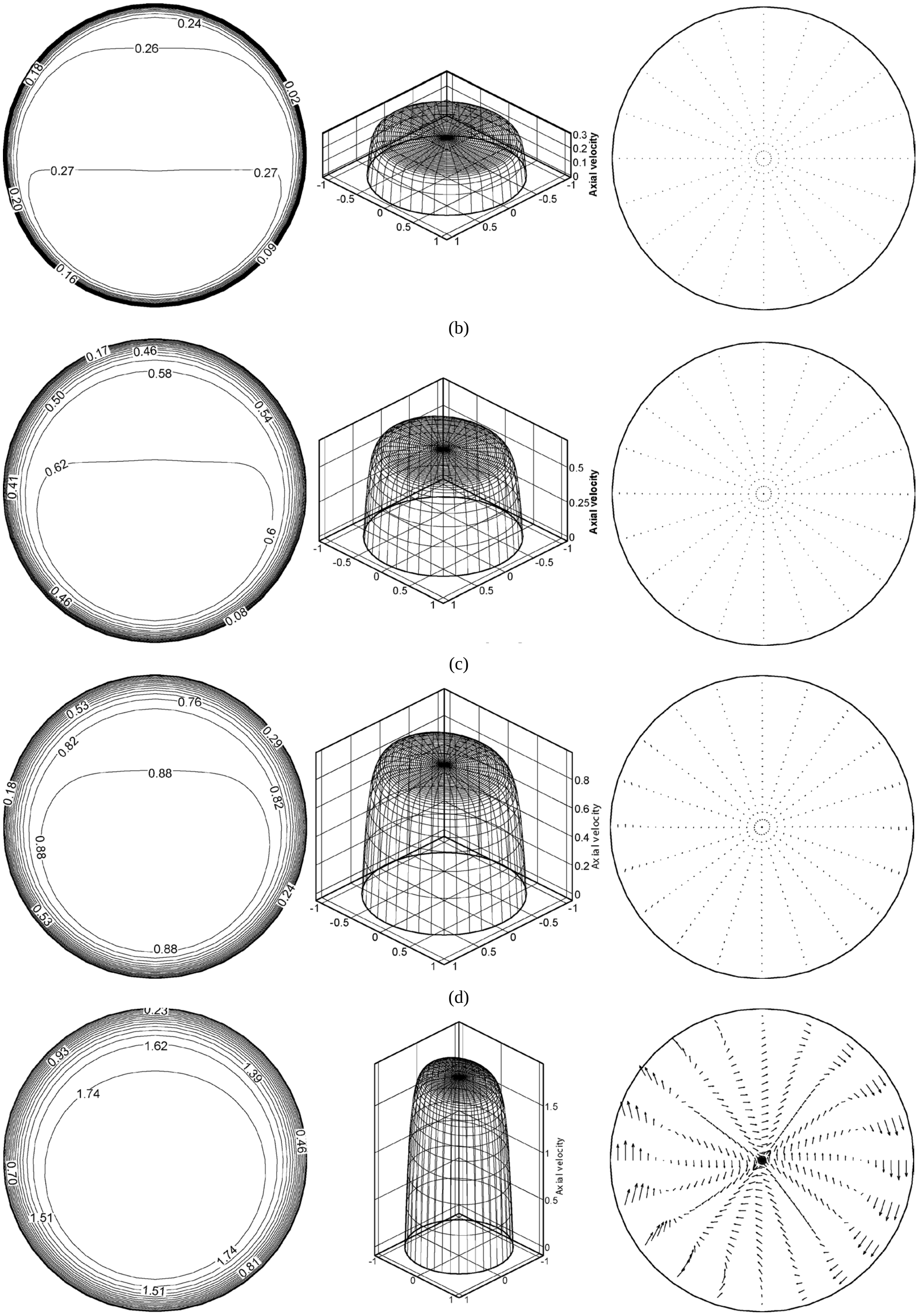

(b)

(c)

(d)

(e)

Fig. 2. Continued.

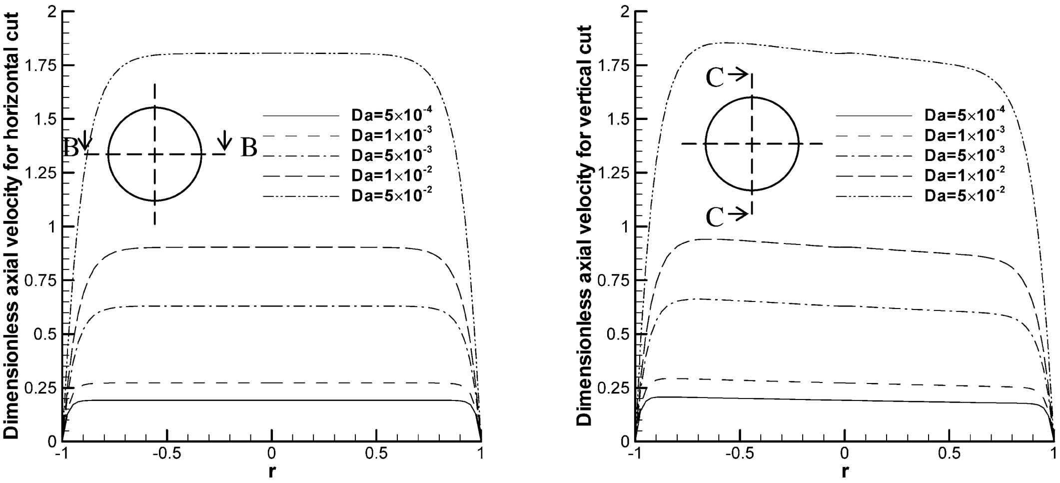

Fig. 3. Axial velocity profiles in the horizontal (left) and vertical (right) cut view of the pipe at $\mathrm{d}P/\mathrm{d}s = -10$, $C_{\mathrm{F}} = 0.55$, $\varphi = 0.95$, $\varepsilon = 0.1$, $\lambda = 0.1$ for different Darcy numbers. The curves for different Da in Fig. 3 correspond to the cases (a)–(e) displayed in Fig. 2: (a) $Da = 5 \times 10^{-4}$, (b) $Da = 1 \times 10^{-3}$, (c) $Da = 5 \times 10^{-3}$, (d) $Da = 1 \times 10^{-2}$, (e) $Da = 5 \times 10^{-2}$.

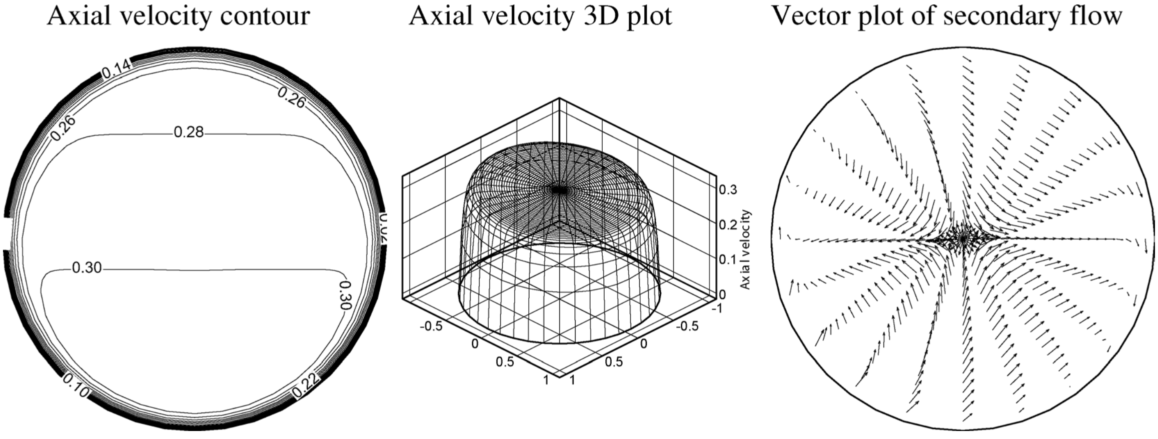

(a)

Fig. 4. Contour lines and 3D plots of the axial velocity and vector plots of the secondary flow at $\mathrm{d}P/\mathrm{d}s = -10$, $Da = 1 \times 10^{-3}$, $\varphi = 0.95$, $\varepsilon = 0.1$, $\lambda = 0.1$ for different Forchheimer coefficients: (a) $C_{\mathrm{F}} = 0.0$, (b) $C_{\mathrm{F}} = 0.25$, (c) $C_{\mathrm{F}} = 0.50$, (d) $C_{\mathrm{F}} = 0.75$, (e) $C_{\mathrm{F}} = 1.0$.

with central differences. The SIMPLE algorithm (Patankar [16]) is utilized on a staggered grid arrangement to solve the governing equations.

A one-dimensional parabolic velocity profile is imposed as the initial guess. Computations are terminated when the convergence criterion is met. The following criterion is adopted

$$\frac{\|\hat{\mathbf{r}}^{(k)}\|_\infty}{\|\hat{\mathbf{r}}^{(0)}\|_\infty} \leqslant 10^{-6}, \tag{3.1}$$

where $\hat{\mathbf{r}}$ is the residual of the pressure correction equation obtained from the continuity equation when using the SIMPLE method. The superscripts (0) and (k) refer to the initial value and kth iteration, respectively. A no-slip boundary condition is assumed at the walls of the helical pipe. In the coordinate system utilized in this research, there is a numerical singularity at the pipe axis ($r = 0$), so boundary values are needed for flow quantities, which are either located directly at the pipe axis or at the opposite sides of the pipe axis (Hüttl [8], Cheng and Kuznetsov [13]).

If an even number of cells in the circumferential direction is used, matching of axial velocities from the opposite sides of the pipe axis can be utilized:

$$u_s\left(s, -\frac{\Delta r}{2}, \theta\right) = u_s\left(s, \frac{\Delta r}{2}, \theta + \pi\right). \tag{3.2}$$

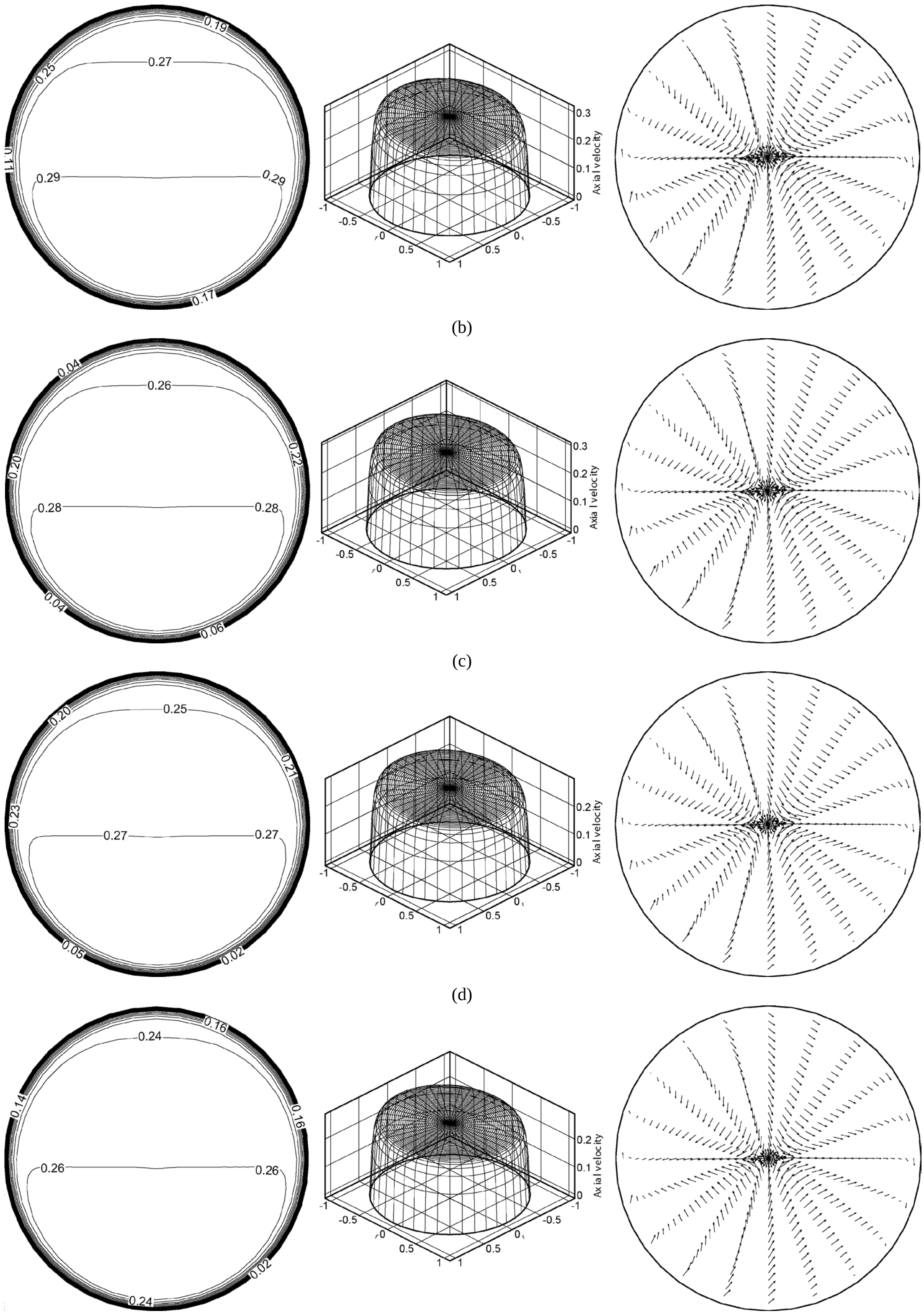

(e)

Fig. 4. Continued.

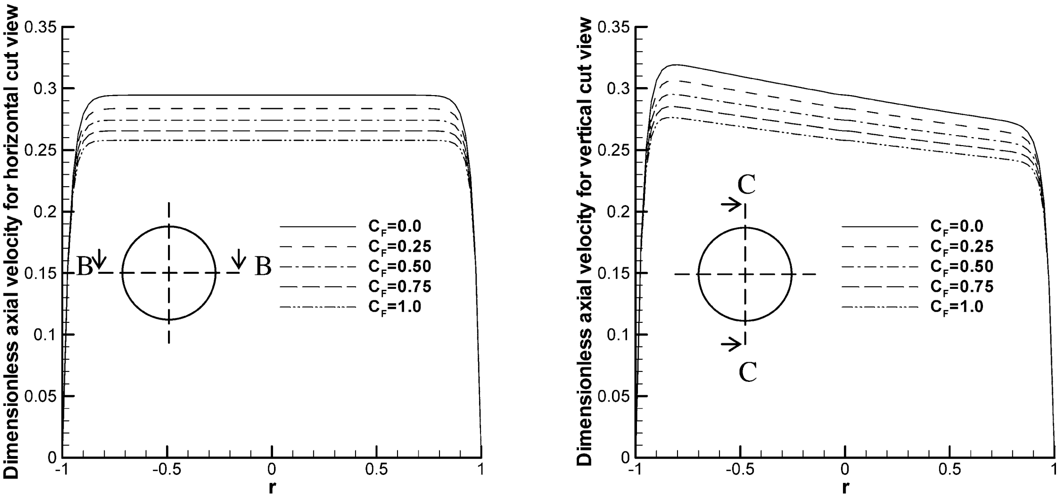

Fig. 5. Axial velocity profiles in the horizontal (left) and vertical (right) cut view of the pipe at $\mathrm{d}P/\mathrm{d}s = -10$, $Da = 1 \times 10^{-3}$, $\varphi = 0.95$, $\varepsilon = 0.1$, $\lambda = 0.1$ for different Forchheimer coefficients. The curves for different C_F in Fig. 5 correspond to the cases (a)–(e) displayed in Fig. 4: (a) $C_\mathrm{F} = 0.0$, (b) $C_\mathrm{F} = 0.25$, (c) $C_\mathrm{F} = 0.50$, (d) $C_\mathrm{F} = 0.75$, (e) $C_\mathrm{F} = 1.0$.

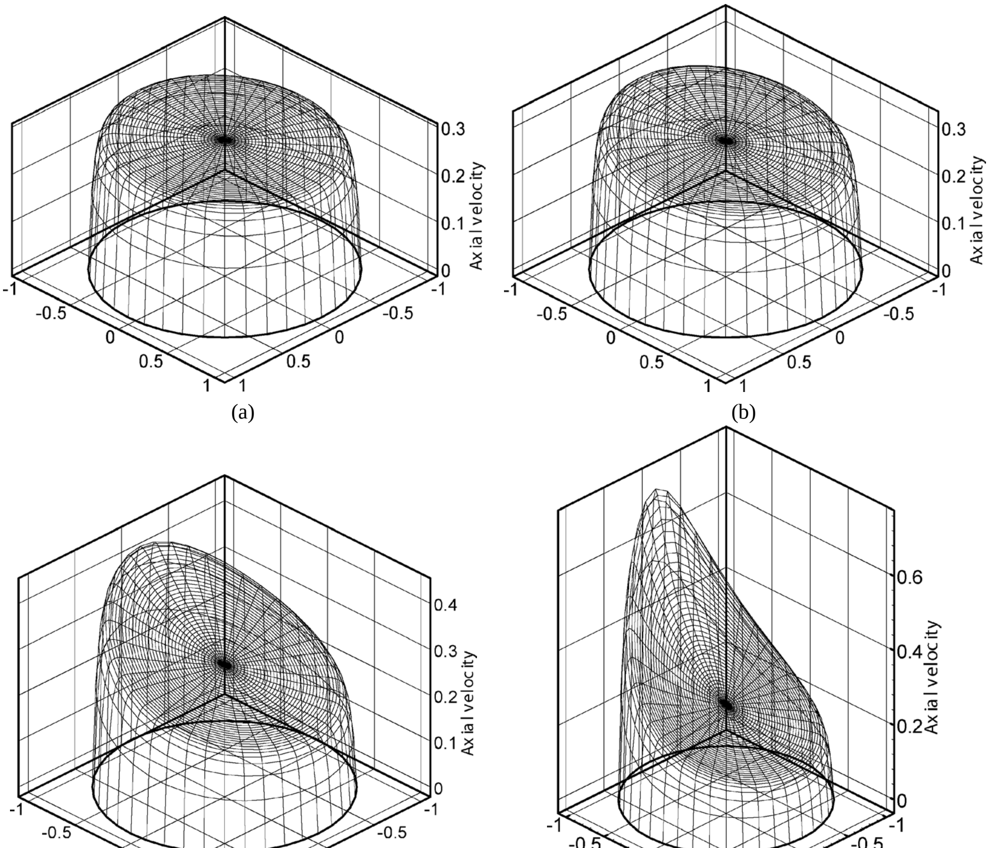

(a) (b)

(c) (d)

Fig. 6. 3D plots of the axial velocity at $\mathrm{d}P/\mathrm{d}s = -10$, $Da = 1 \times 10^{-3}$, $C_\mathrm{F} = 0.55$, $\varphi = 0.95$, $\lambda = 0.1$ for different dimensionless curvatures: (a) $\varepsilon = 0.1$, (b) $\varepsilon = 0.2$, (c) $\varepsilon = 0.5$, (d) $\varepsilon = 0.8$.

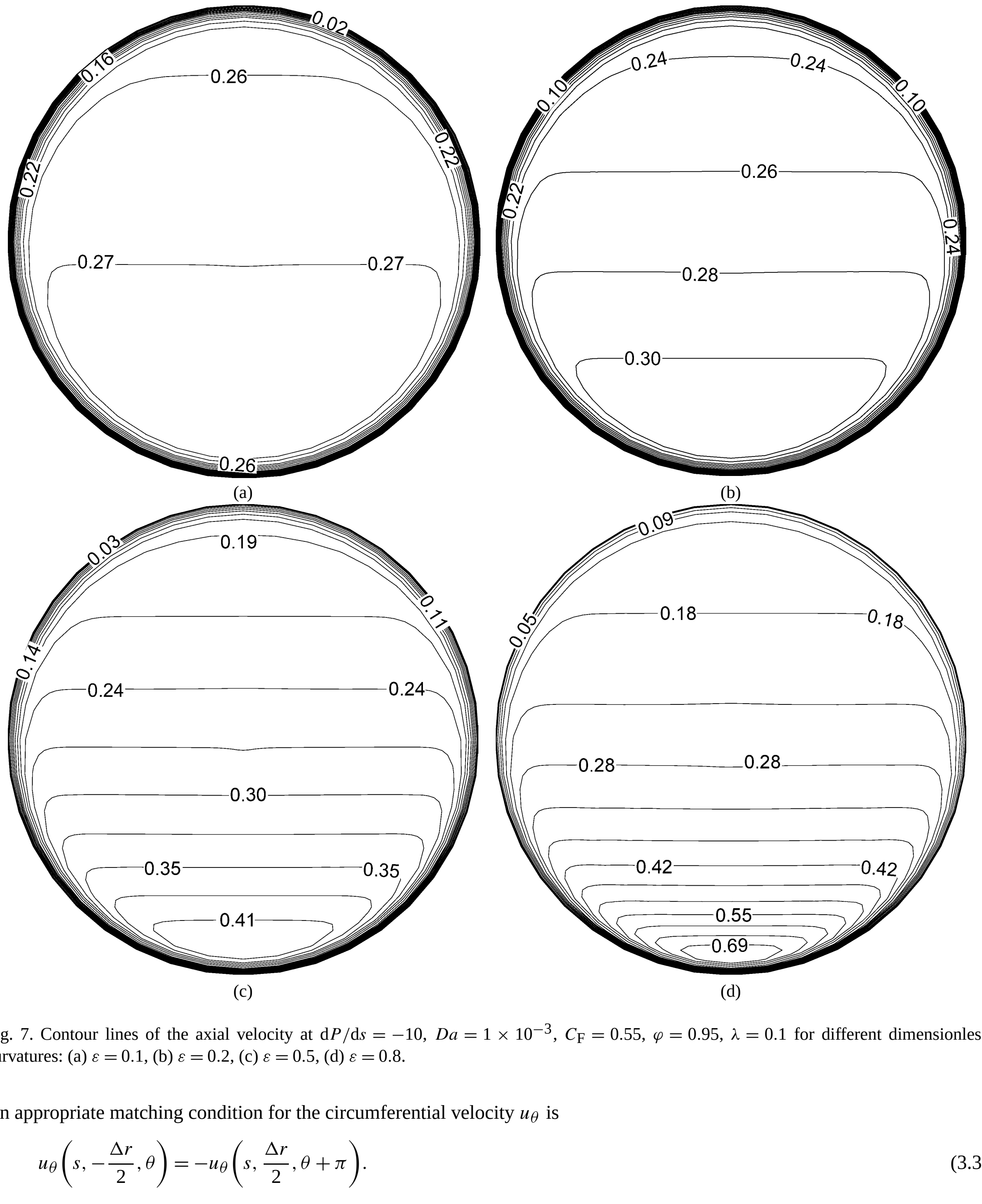

(a) (b)

(c) (d)

Fig. 7. Contour lines of the axial velocity at $\mathrm{d}P/\mathrm{d}s = -10$, $Da = 1 \times 10^{-3}$, $C_{\mathrm{F}} = 0.55$, $\varphi = 0.95$, $\lambda = 0.1$ for different dimensionless curvatures: (a) $\varepsilon = 0.1$, (b) $\varepsilon = 0.2$, (c) $\varepsilon = 0.5$, (d) $\varepsilon = 0.8$.

An appropriate matching condition for the circumferential velocity u_θ is

$$u_\theta\left(s, -\frac{\Delta r}{2}, \theta\right) = -u_\theta\left(s, \frac{\Delta r}{2}, \theta + \pi\right). \tag{3.3}$$

The minus sign is due to the fact that the direction of the circumferential velocity at θ is defined opposite of that at $\theta + \pi$. The value of the radial velocity at the pipe axis is determined by a linear interpolation across the axis:

$$u_r(s, r = 0, \theta) = \frac{u_r(s, \Delta r, \theta) - u_r(s, \Delta r, \theta + \pi)}{2}. \tag{3.4}$$

The minus sign results from the fact that the coordinate direction changes for the radial velocity when taking the value from the opposite side.

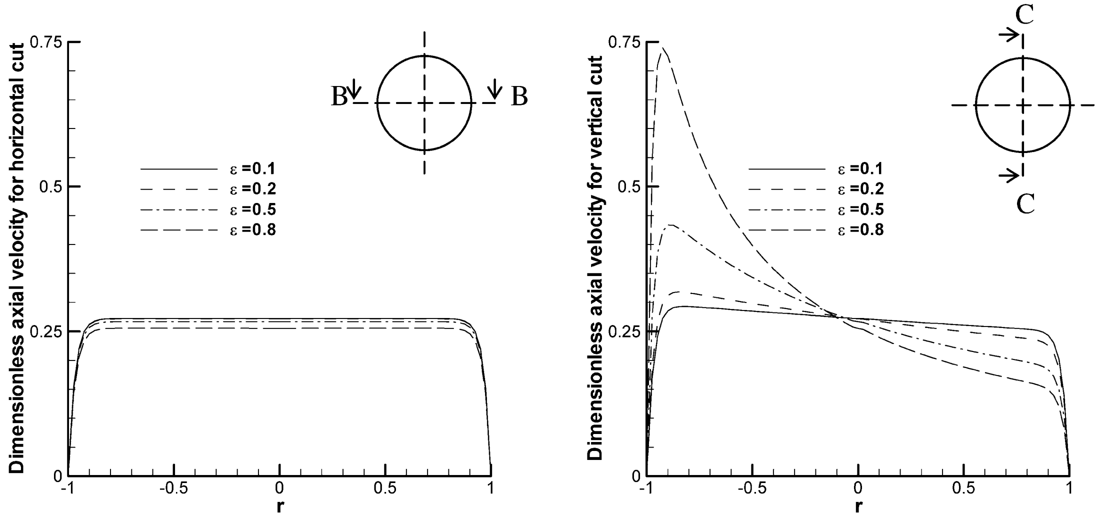

Fig. 8. Axial velocity profiles in the horizontal (left) and vertical (right) cut view of the pipe at $\mathrm{d}P/\mathrm{d}s = -10$, $Da = 1 \times 10^{-3}$, $C_\mathrm{F} = 0.55$, $\varphi = 0.95$, $\lambda = 0.1$ for different dimensionless curvatures. The curves for different ε in Fig. 8 correspond to the cases (a)–(d) displayed in Figs. 6 and 7: (a) $\varepsilon = 0.1$, (b) $\varepsilon = 0.2$, (c) $\varepsilon = 0.5$, (d) $\varepsilon = 0.8$.

An initial value of the Reynolds number, which is needed to start iterations, is estimated as follows. The flow is driven by a constant pressure gradient $\mathrm{d}\widetilde{P}/\mathrm{d}\tilde{s}$ that has to balance the fluid friction in a porous medium. If fluid friction was modeled by only the Darcian resistance, the axial pressure gradient would be estimated as

$$\frac{\mathrm{d}\widetilde{P}}{\mathrm{d}\tilde{s}} = -\frac{\mu}{k}\tilde{u}_s. \tag{3.5}$$

This gives the following equation that relates the dimensionless pressure gradient and the Reynolds number defined in Eq. (2.9)

$$\frac{\mathrm{d}P}{\mathrm{d}s} = -\frac{1}{Da\,Re}. \tag{3.6}$$

This is used to evaluate only the initial value of *Re*. During the iteration process, *Re* is evaluated according to Eq. (2.9) utilizing the value of the mean velocity from the previous iteration.

4. Results and discussion

This paper investigates the fully-developed laminar flow in a helical pipe filled with a fluid saturated porous medium driven by a constant pressure gradient. Fig. 2 displays the axial velocity contours, axial velocity profiles and velocity vector plot of the secondary flow in the plane normal to the main flow at different Darcy numbers. It shows that the axial velocity increases with the Darcy number. This is because a larger Darcy number means larger permeability, which results in larger filtration velocity. The axial velocity profiles show that when the Darcy number is very small, the profile of the axial velocity is almost that of a slug flow. The effect of the centrifugal force that is usually important in helical pipe flow can not be observed. With an increase of the Darcy number, the distortion of the velocity profile becomes apparent and the maximum axial velocity is displaced towards the outer wall. The effect of the Darcy number on secondary flow is also significant. For small Darcy numbers, the secondary flow can not be seen but when the Darcy number is increased to 5×10^{-2}, the secondary flow becomes very strong. The axial velocity profiles for the horizontal and vertical cut view at different Darcy numbers are plotted in Fig. 3. It clearly shows the trend of the axial velocity described above when the Darcy number changes.

Fig. 4 displays the effects of the Forchheimer coefficient, C_F, on the fluid flow in a helical pipe filled with a porous medium. The contour lines and the 3D plots of the axial velocity show that the distributions of the axial velocity are similar for different values of C_F except that the value of the axial velocity decreases with C_F. A larger Forchheimer coefficient means larger form drag due to solid obstacles in the porous medium, therefore, the axial velocity decreases when C_F increases. The secondary flow is also damped a little for larger Forchheimer coefficients, as shown in the vector plots of the secondary flow. Fig. 5 shows the profiles of the axial velocity for both the horizontal and vertical cut view of a cross-section normal to the pipe axes. The distortion of the axial velocity profile is observed for all displayed cases. The velocity profiles in the core region of the pipe (outside the boundary layer region) computed for different values of the Forchheimer coefficient are parallel to each other.

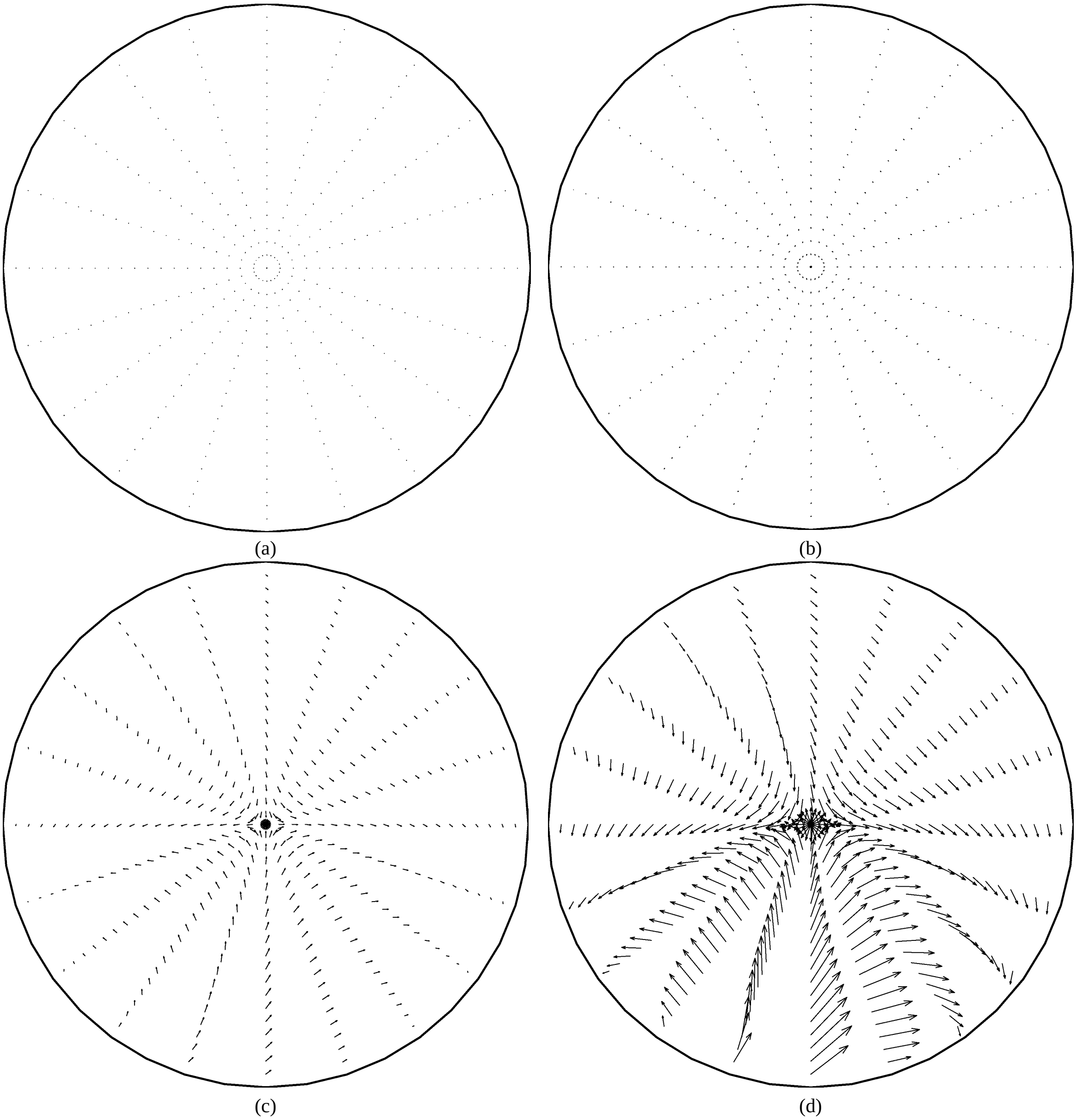

Fig. 9. Vector plots of secondary flow at $\mathrm{d}P/\mathrm{d}s = -10$, $Da = 1 \times 10^{-3}$, $C_F = 0.55$, $\varphi = 0.95$, $\lambda = 0.1$ for different dimensionless curvatures: (a) $\varepsilon = 0.1$, (b) $\varepsilon = 0.2$, (c) $\varepsilon = 0.5$, (d) $\varepsilon = 0.8$.

Figs. 6–8 and 9 present the effect of the dimensionless curvature, ε, on the distribution of the axial velocity. Both 3D (Fig. 6) and 2D (Fig. 7) plots of the axial velocity show that when ε increases, the maximum axial velocity is displaced to the outer wall and the value of the maximum axial velocity increases. Fig. 8 presents profiles of the axial velocity for the horizontal and vertical cut view. It is interesting that the profiles are quite flat for the horizontal cut view and are relatively independent of ε; the profile for the vertical cut view, however, is inclined to the outer wall and becomes steeper when the dimensionless curvature, ε, increases. The profile of the axial velocity becomes cuneiform for the case of $\varepsilon = 0.8$. The vector plots of the secondary flow displayed in Fig. 9 show that the secondary flow is almost invisible for the case of $\varepsilon = 0.1$ but when ε increases the secondary flow becomes much stronger.

Fig. 10 compares the contour lines of the axial velocity, vector plots of the secondary flow, contour lines of the circumferential velocity and the radial velocity for different ratios of torsion to curvature, λ, (0.1, 0.5, and 1.0, respectively) when $\mathrm{d}P/\mathrm{d}s$ is fixed at -10, Darcy number Da is 1×10^{-3}, Forchheimer coefficient C_F is 0.55, φ is 0.95, and ε is fixed at 0.1. The

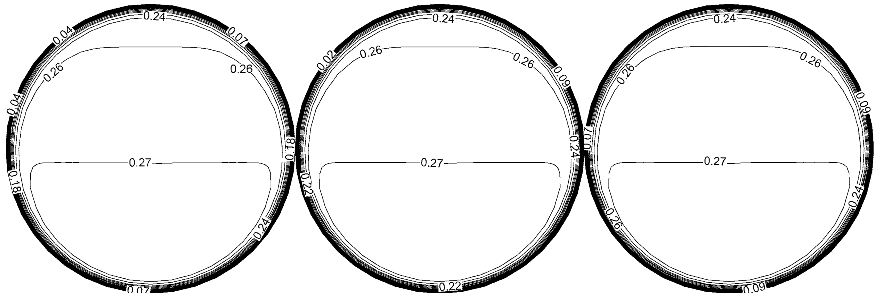

Contour lines of the axial velocity

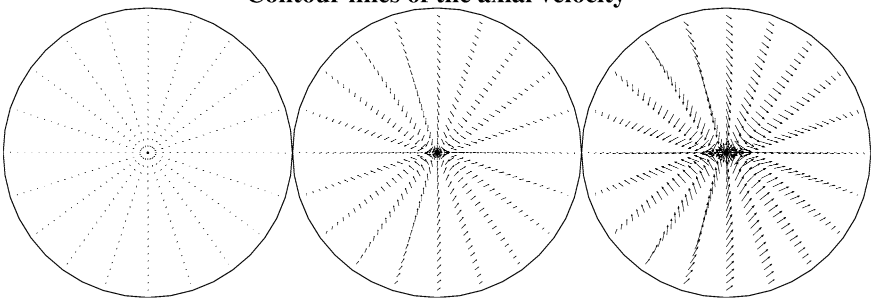

Vector plot of the secondary flow

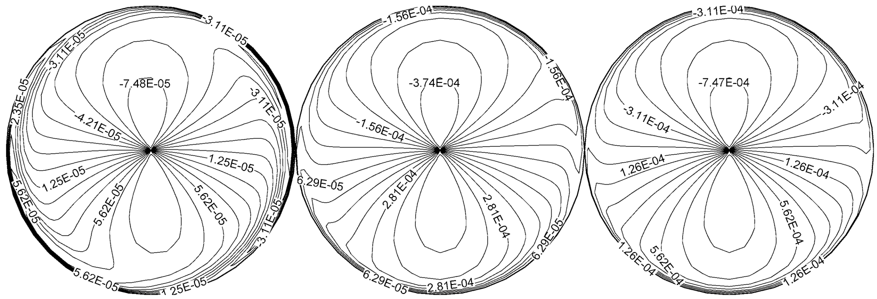

Contour lines of the circumferential velocity

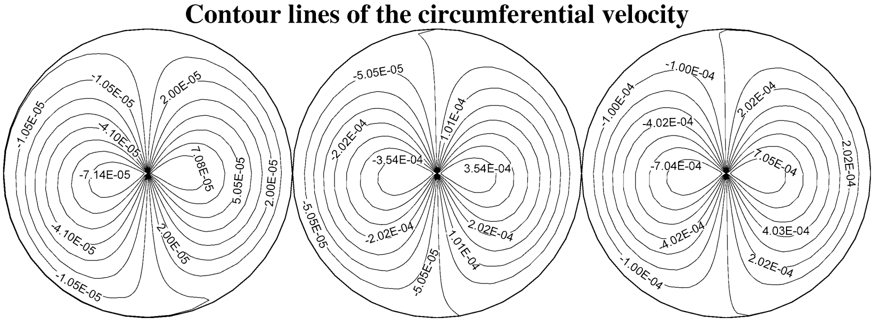

Contour lines of the radial velocity

(a) **(b)** **(c)**

Fig. 10. Velocity components computed for $\mathrm{d}P/\mathrm{d}s = -10$, $Da = 1 \times 10^{-3}$, $C_{\mathrm{F}} = 0.55$, $\varphi = 0.95$, $\varepsilon = 0.1$ for different values of the ratio of torsion to curvature: (a) $\lambda = 0.1$, (b) $\lambda = 0.5$, (c) $\lambda = 1.0$.

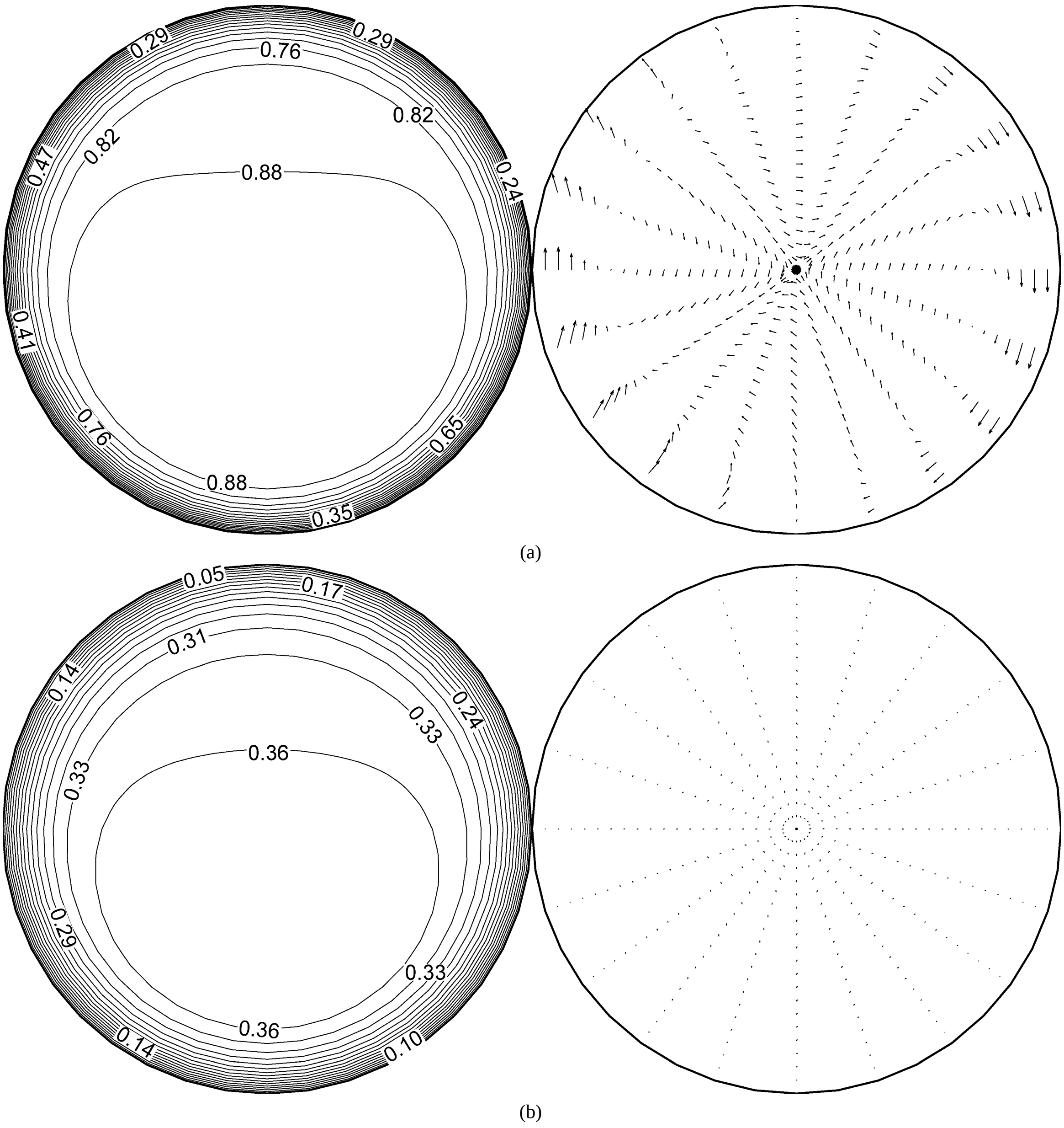

(a)

(b)

Fig. 11. Axial velocity (left) and secondary flow (right) computed for $\mathrm{d}P/\mathrm{d}s = -10$, $Da = 1 \times 10^{-2}$, $C_F = 0.55$, $\varphi = 0.95$, $\varepsilon = 0.1$, $\lambda = 0.1$ utilizing (a) the full momentum equation (with the inertia term) (b) truncated form of the momentum equation (without the inertia term).

contour lines of the axial velocity are similar for the three cases computed with different values of λ and the distributions and magnitudes of the axial velocity are almost identical. It seems that λ does not have much influence on the axial velocity. Nevertheless, the vector plots of the secondary flow depend upon λ. When the ratio of torsion to curvature increases, the secondary flow becomes stronger. The contour lines of the circumferential velocity and radial velocity also show that the magnitudes of velocity components in the plane normal to the main flow increase with λ. However, the magnitudes of circumferential and radial velocity are very small compared to that of the axial velocity.

To show the importance of the inertia term for predicting the secondary flow, Fig. 11 presents computational results obtained using the full form of the momentum equation (with flow inertia) and the truncated form of the momentum equation (with the inertia term neglected). This figure shows that when the inertia term is accounted for in the momentum equation, the axial velocity is greater and the secondary flow is apparent. When the inertia term is neglected, the secondary flow can not be observed.

5. Conclusions

The laminar flow in a helical pipe filled with a fluid saturated porous medium is investigated. A full momentum equation that accounts for the Brinkman and Forchheimer extensions of the Darcy law and the flow inertia is utilized. The governing equations are projected on an orthogonal helical coordinate system. The objective is to study the effects of the parameters characterizing the porous medium, the Darcy number, Da, and the Forchheimer coefficient, C_F, and the geometrical parameters of helical pipes, dimensionless curvature, ε, and the ratio of torsion to curvature, λ. For a given helical pipe, if the Forchheimer coefficient is constant, increasing the Darcy number results in larger axial filtration velocity and the distortion of the axial velocity profile caused by the centrifugal force becomes more apparent. A maximum axial velocity is displaced towards the outer wall. The secondary flow is also intensified with increase in the Darcy number. When Da is fixed, the axial velocity decreases and the secondary flow becomes weaker when the Forchheimer coefficient, C_F, increases. In the core region of the helical pipe, the profiles of the axial velocity are represented by straight lines which are parallel to each other for different values of the Forchheimer coefficient. When Da and C_F are fixed, investigation shows that the dimensionless curvature, ε, affects both the axial velocity distribution and the secondary flow, but the other dimensionless parameter, the ratio of torsion to curvature, λ, affects only the secondary flow. When ε increases, the flow through the helical pipe is dragged more to the outer wall and the profile of the axial velocity changes from flat to cuneiform. The secondary flow is not visible for small ε, but becomes stronger when ε increases. The larger ratio of torsion to curvature, λ, results in stronger secondary flow but does not significantly affect the distribution of the axial velocity. Computations utilizing the truncated form of the momentum equation (with the inertia term neglected) show that accounting for the inertia term is crucial for predicting secondary flow in a helical pipe. Thus, in a curved pipe, utilizing the Brinkman–Forchheimer extension of the Darcy law is insufficient to correctly predict the secondary flow. The inertia term must be accounted for as well.

References

[1] W.R. Dean, Note on the motion of fluid in a curved pipe, Philos. Magazine 4 (1927) 208–223.
[2] M. Germano, On the effect of torsion on a helical pipe flow, J. Fluid Mech. 125 (1982) 1–8.
[3] M. Germano, The Dean equations extended to a helical pipe flow, J. Fluid Mech. 203 (1989) 289–305.
[4] S. Liu, J.H. Masliyah, Axially invariant laminar flow in helical pipes with a finite pitch, J. Fluid Mech. 251 (1993) 315–353.
[5] S. Liu, J.H. Masliyah, Developing convective heat transfer in helical pipes with finite pitch, Int. J. Heat Fluid Flow 15 (1994) 66–74.
[6] G. Yang, Z.F. Dong, M.A. Ebadian, Laminar forced convection in a helicoidal pipe with finite pitch, Int. J. Heat Mass Transfer 38 (1995) 853–862.
[7] T.J. Hüttl, Navier Stokes solutions of laminar flows based on orthogonal helical coordinates, Numer. Methods in Laminar and Turbulent Flow 10 (1997) 191–202.
[8] T.J. Hüttl, Influence of curvature and torsion on turbulent flow in curved and helically coiled pipes, Int. J. Heat Fluid Flow 21 (2000) 345–353.
[9] J.G. Pharoah, S. Litster, N. Djilali, Mass transfer enhancement in membrane separation–rotating vs. helical modules, in: CFD 2003, Vancouver, May, 2003, pp. 28–30.
[10] B. Zheng, C.X. Lin, M.A. Ebadian, Combined laminar forced convection and thermal radiation in a helical pipe, Int. J. Heat Mass Transfer 43 (2000) 1067–1078.
[11] C.X. Lin, P. Zhang, M.A. Ebadian, Laminar forced convection in the entrance region of helical pipes, Int. J. Heat Mass Transfer 40 (1997) 3293–3304.
[12] K.P. Sandeep, C.A. Zuritz, V.M. Puri, Modeling non-Newtonian two-phase flow in conventional and helical-holding tubes, Int. J. Food Sci. Technol. 35 (2000) 511–522.
[13] L. Cheng, A.V. Kuznetsov, Investigation of a laminar flow of a non-Newtonian fluid in a helical pipe. Int. J. Appl. Mech. Engrg., in press.
[14] D.A. Nield, A.V. Kuznetsov, Forced convection in a helical pipe filled with a saturated medium, Int. J. Heat Mass Transfer 47 (2004) 5175–5180.
[15] D.A. Nield, A. Bejan, Convection in Porous Media, second ed., Springer, New York, 1999.
[16] S.V. Patankar, Numerical Heat Transfer and Fluid Flow, Hemisphere, New York, 1980.